Magnetic phases and unusual topological electronic structures of Weyl semimetals in strong interaction limit

Liang-Jun Zhai,[1,2] Po-Hao Chou,[1] and Chung-Yu Mou[1,3,4]

[1]*Department of Physics, National Tsing Hua University, Hsinchu 30013, Taiwan, Republic of China*

[2]*The School of Mathematics and Physics, Jiangsu University of Technology, Changzhou 213001, China*

[3]*Institute of Physics, Academia Sinica, Nankang 115, Taiwan, Republic of China*

[4]*Physics Division, National Center for Theoretical Sciences, P.O. Box 2-131, Hsinchu 30013, Taiwan, Republic of China*

(Received 23 May 2016; revised manuscript received 9 August 2016; published 20 September 2016)

The interplay of electronic band structures and electron-electron interactions is known to develop new phases in condensed matter. In this paper, we investigate the thermodynamic phases and corresponding electronic structures of a Weyl semimetal in a strong on-site Coulomb interaction limit. Based on a minimum model of a Weyl semimetal with two linear Weyl nodes, it is shown that generically the Weyl semimetal becomes magnetic in the presence of interactions. In particular, it is shown that the Dzyaloshinskii-Moriya exchange interaction is generally induced so that the A-type antiferromagnetic (A-AFM) phase and the spiral spin density wave (SSDW) states are two generic phases. Furthermore, we find that Weyl nodes proliferate and it is possible to doubly enhance the unusual properties of noninteracting Weyl semimetals through the realization of double-Weyl nodes in a strong correlation limit. Specifically, it is shown that in the SSDW phase, linear Weyl nodes are tuned into double-Weyl nodes with the corresponding charges being ± 2. As the spin-orbit coupling increases, a quantum phase transition occurs with the SSDW phase being turned into an A-AFM phase and, at the same time, double-Weyl nodes are disintegrated into two pairs of linear Weyl nodes. Our results reveal the unusual interplay between the topology of electronic structures and magnetism in strongly correlated phases of Weyl semimetals.

DOI: 10.1103/PhysRevB.94.125135

I. INTRODUCTION

Since the discovery of the time-reversal (TR) invariant topological insulator (TI) in two dimensions (2D) and three dimensions (3D) [1,2], the topological aspects of the electronic band structures have become important benchmarks to characterize electronic phases in condensed matter physics. The unique feature of TIs lies in their properties being insulating in the bulk, and yet their surfaces are metallic due to the existence of surface states. The surface states result from the nontrivial topology of the bulk band structure and are robust against perturbations that respect the symmetries of the system. More recently, it is further realized that even if the band structures of the materials are gapless, nontrivial topology of the gapless points (nodal points) may also result in topologically protected surface states [3].

Among the class of topological gapless materials, the Dirac semimetal and the Weyl semimetal are the simplest types, characterized by the presence of nodal points at which two distinct bands touch [4–9]. For the Dirac semimetal, the low-energy Hamiltonian near the isolated Dirac nodes can be described by the Dirac equation with both time-reversal symmetry and inversion symmetry being preserved, and it can be realized in both 2D and 3D systems, such as graphene (2D) [8] and Na_3Bi (3D) [10]. In contrast, the time-reversal symmetry or inversion symmetry is explicitly broken in the Weyl semimetal, and the Hamiltonian around the Weyl nodes is described by the Weyl Hamiltonian given by $H = \pm v_F \boldsymbol{\sigma}\cdot\mathbf{k}$, with $\boldsymbol{\sigma}$ the Pauli matrices and $\mathbf{k}$ the momentum deviation from the Weyl point, and $\pm$ denotes the chirality. The absence of time-reversal symmetry or inversion symmetry results in the separation of Weyl nodes either in momentum or in energy. In addition, it results in nontrivial topology (chirality) carried by the Weyl nodes, which is characterized by the monopole charges Q defined as the integral of the Berry curvature $\boldsymbol{\Omega}(\boldsymbol{k})$ over the surface enclosing the node, $Q = (1/2\pi)\oint d\boldsymbol{S}_{\boldsymbol{k}}\cdot\boldsymbol{\Omega}(\boldsymbol{k})$ [11]. Due to the topological nature of Q, Weyl fermions in these materials are robust to small perturbations [12,13]. For large perturbations, it is known that localized states may arise near the point defects [14] and Weyl points can even appear or disappear in pairs with opposite monopole charges. In the simple Weyl semimetals, each Weyl point carries $Q = 1$ or $Q = -1$, which has been first realized experimentally in TaAs [15]. The possibility of multiple Weyl nodes with $|Q| > 1$ has also been recently proposed [16–18]. Instead of being the usual linear Weyl nodes carrying a ± 1 monopole charge, the multiple Weyl nodes, protected by C_4 or C_6 rotation symmetry, have a nonlinear dispersion and higher monopole charge. The lowest nontrivial example is the double-Weyl semimetal with $Q = \pm 2$, which is suggested to be realized in the 3D semimetal $HgCr_2Se_4$ [17]. The double-Weyl nodes possess quadratic dispersions in two directions, e.g., the xy plane and linear dispersion in the third direction. Furthermore, it is known that due to the presence of larger chiral charges Q, the unusual phenomena (such as quantum anomalous Hall conductivity, chiral anomaly, and the number of Fermi arcs) associated with the linear Weyl nodes are doubly enhanced [18–20].

While the above-mentioned properties are valid for noninteracting Weyl semimetals, it is known that nontrivial topology in an electronic structure is driven by a spin-orbit interaction, which inevitably involves heavy elements. Correlation effects due to the interactions are therefore present and it is necessary to examine the effects of the interactions on the properties of Weyl semimetals. For topological insulators, the Coulomb interaction is usually screened and becomes short ranged. Studies indicate that topological transitions may be induced so that nontrivial topological phases may be broken into

topologically trivial phases by a sufficiently strong short-range correlation [9,21–24]. On the other hand, for Dirac/Weyl semimetals, the long-range Coulomb interaction is shown to be marginally irrelevant and induces logarithmic corrections in the response functions [9,18,20,25]. In the strong-coupling limit, however, the semimetals could be turned into either a Mott insulator if the nodal point is anisotropic [26] or a charge density wave (CDW) state [27]. Since in typical materials that realize Dirac/Weyl semimetals, localized electronic orbits, such as the *d* orbits in Ta of TaAs, are often involved, the on-site Coulomb energy in the materials usually dominates. Therefore, it would be interesting and necessary to investigate the effects of short-ranged Coulomb interactions on Weyl semimetals.

In this paper, we examine the phases of a Weyl semimetal in the presence of an on-site Coulomb interaction in a Hubbard model. Similar to the effects of disorders [12], in the weak interacting regime, it is found that the Weyl semimetal is paramagnetic without magnetic orders. The electronic structure is similar to that of noninteracting Weyl fermions with the parameters being renormalized. As the on-site interaction increases and is strong enough, the Weyl semimetal becomes magnetic. In the strong interaction limit of a Hubbard model, we find that the A-type antiferromagnetic (A-AFM) phase and the spin density wave (SSDW) phase are two generic phases. In the SSDW phase, each Weyl node is turned into a double-Weyl node with the corresponding charge being ± 2. As the spin-orbit coupling increases, a first-order phase transition occurs with the SSDW phase being turned into an A-AFM phase and, at the same time, double-Weyl nodes disintegrate into two pairs of linear Weyl nodes. Our results reveal the unusual interplay between the topology of the electronic structures and magnetism in the strongly correlated phases of Weyl semimetals and pave a way for realizing a double-Weyl semimetal based on linear Weyl semimetals.

The rest of the paper is organized as follows. In Sec. II, the model of a Weyl semimetal with a Hubbard interaction is introduced. By using a canonical transformation, we derive the effective low-energy Hamiltonian for the strong-coupling limit of the Hubbard model. Under the Gutzwiller approximation, a renormalized mean-field Hamiltonian is constructed. In Sec. III, magnetic phases in the strong Coulomb interaction limit are solved numerically. It is shown that the corresponding electronic structures possess nontrivial nodal structures. Finally, in Sec. IV, we conclude and discuss. How our results change from the weak interaction regime to the strong-coupling regime is presented and discussed. A possible connection of our results to experimental observations is also presented.

II. THEORETICAL MODEL OF WEYL SEMIMETAL

We start with a minimum model of a 3D Weyl semimetal on a simple cubic lattice [28] with an on-site Hubbard repulsion interaction U. The model has a minimum number of two Weyl points. Since the on-site Hubbard U interaction is rotationally invariant, two Weyl points can be chosen to be along the z axis so that the Hamiltonian is given by

$$H = \sum_{\mathbf{k},\alpha,\beta} C^{\dagger}_{\alpha}(\mathbf{k}) H_{0,\alpha\beta}(\mathbf{k}) C_{\beta}(\mathbf{k}) + U \sum_{i} \hat{n}_{i\uparrow}\hat{n}_{i\downarrow}, \tag{1}$$

with H_0 being a 2×2 matrix,

$$H_0(\mathbf{k}) = (t_1 \cos k_z - \mu)\sigma_0 + t_2(m + 2 - \cos k_x - \cos k_y)\sigma_z + t_{\mathrm{so}} \sin \mathbf{k} \cdot \boldsymbol{\sigma}. \tag{2}$$

Here, α and β take $\uparrow$ or $\downarrow$ that represent the spin up or spin down, and $C^{\dagger}_{\alpha}$ creates an electron with spin up or spin down. Also, $\sin \mathbf{k} \cdot \boldsymbol{\sigma}$ is shorthand notation for $\sigma_x \sin k_x + \sigma_y \sin k_y + \sigma_z \sin k_z$. t_1 and t_2 represent the hopping amplitudes along the z direction and in the xy plane, respectively. t_{so} is the strength of the spin-orbit coupling and m is the exchange parameter that controls the degree of time-reversal symmetry breaking. m will be set to zero in most of the following computations. μ is the chemical potential, and σ_0 is the 2×2 identity matrix. Finally, U describes the on-site Hubbard repulsion interaction. The model, Eq. (2), is an extension of the Qi-Wu-Zhang (QWZ) model in the study of the 2D quantum anomalous Hall effect [29] and it has only two Weyl nodes at the ground state with $U = 0$ and $m = 0$ [28].

In the case of $U = 0$, the system has a C_4 rotation symmetry, and the nonzero t_1 would break the space inversion symmetry with respect to the x-y plane, while the t_2 term breaks the time-reversal symmetry. The energies of the two bands can be solved and are given by

$$E_{\pm}(\mathbf{k}) = t_1 \cos k_z \pm \sqrt{t_{\mathrm{so}}^2(\sin^2 k_x + \sin^2 k_y) + [t_{\mathrm{so}} \sin k_z + t_2(m + 2 - \cos k_x - \cos k_y)]^2}. \tag{3}$$

The ground state of this minimum model has been well studied in Ref. [28]. By tuning the values of m and t_{so}, the ground state of the two-band model could be either in a topological trivial phase or the Weyl semimetal phase.

When U is switched on and is small, the free-energy gain due to magnetic orders is also small. One thus expects that the Weyl semimetal is paramagnetic without magnetic orders. Hence the electronic structure is similar to that of noninteracting Weyl fermions with the parameters being just renormalized. As U increases, the free-energy gain due to magnetic orders also increases. As a result, only when U is strong enough does the Weyl semimetal start to become magnetic. Therefore, we shall first consider the strong interaction limit when U is large. The connection of the strong-U limit to the weak-U limit will be discussed later.

In the strong interaction limit when U is large, the band structure resulting from Eq. (1) can be very different from that for $U = 0$. In the large-U limit, the Hilbert space is energetically decomposed into singly occupied and doubly occupied spaces so that the electron operator can be decomposed as $C^{\dagger}_{i\sigma} = C^{\dagger}_{i\sigma}(1 - n_{i,-\sigma}) + C^{\dagger}_{i\sigma} n_{i,-\sigma}$. Since only the kinetic energy, $T \equiv \sum_{i,j} C^{\dagger}_i H_{0,ij} C_j$, mixes singly occupied and doubly occupied spaces, we first perform a canonical transformation on the Hamiltonian H to eliminate

the mixing term. If the canonical transformation is generated by S, the transformed Hamiltonian H' is given by

$$H' = e^{iS} H e^{-iS} = H + [iS, H] + [iS, [iS, H]] + \cdots . \quad (4)$$

The mixing terms in the kinetic energy can be written as a summation of T_{+1} and T_{-1} with

$$T_{+1} = \sum_{i,j,\alpha,\beta} C^{\dagger}_{i,\alpha} n_{i,-\alpha} H_{0,ij,\alpha,\beta} C_{j,\beta} (1 - n_{i,-\beta}),$$
$$T_{-1} = \sum_{i,j,\alpha,\beta} C^{\dagger}_{i,\alpha} (1 - n_{i,-\alpha}) H_{0,ij,\alpha,\beta} C_{j,\beta} n_{i,-\beta}. \quad (5)$$

By requiring $T_{+1} + T_{-1} + [iS, H_U] = 0$, one can eliminate the mixing term to first order in U. Here, $H_U = U \sum_i \hat{n}_{i\uparrow} \hat{n}_{i\downarrow}$, and we find

$$iS = \frac{1}{U}(T_{+1} - T_{-1}). \quad (6)$$

Substituting iS in Eq. (6) back to Eq. (4) and keeping the lowest-order terms, after some algebra, we find that the low-energy Hamiltonian is an extended t-J model which can be generally expressed as $H_{\text{eff}} = H_t + H_J$ with [30] H_t and H_J given by

$$H_t = \sum_{i\delta_z,\sigma} t_1 \tilde{C}^{+}_{i,\sigma} \tilde{C}_{i+\delta_z\sigma} + \sum_{i\delta_x(y),\sigma} \sigma t_2 \tilde{C}^{+}_{i,\sigma} \tilde{C}_{i+\delta_{x(y)}\sigma} - \frac{i}{2} t_{\text{so}} \sum_{ij,\sigma\sigma'} \sigma \tilde{C}^{+}_{i,\sigma} \tilde{C}_{j\overline{\sigma'}} + \text{H.c.} \quad (7)$$

and

$$H_J = \sum_{i,\delta_{x(y)}} \left(- J_b S^x_i S^x_{i+\delta_{x(y)}} - J_a S^y_i S^y_{i+\delta_{x(y)}} + J_b S^z_i S^z_{i+\delta_{x(y)}} - \frac{1}{4} J_1 n_i n_{i+\delta_{x(y)}} \right) + \sum_{i,\delta_z} \left[J^1_z \left(S^x_i S^x_{i+\delta_z} + S^y_i S^y_{i+\delta_z} \right) + J^2_z \left(S^z_i S^z_{i+\delta_z} - \frac{1}{4} n_i n_{i+\delta_z} \right) + J_2 \delta_z \cdot S_i \times S_{i+\delta_z} \right]. \quad (8)$$

Here, H_t and H_J represent the hopping and exchange magnetic interactions of the Hamiltonian. $S^{\alpha}_i = \sum_{\sigma\sigma'} \tilde{C}^{+}_{i\sigma} \sigma_{\alpha} \tilde{C}_{i\sigma'}$ ($\alpha = x, y, z$) is the spin operator on site i, and $\delta_{\alpha} = (r_j - r_i)_{\alpha}$ ($\alpha = x, y, z$) represents the vector connecting the sites in the nearest neighbors, with r_i being the position of the lattice site i. $\tilde{C}_{i\sigma} = (1 - n_{i,-\sigma}) C_{i\sigma}$ satisfies the no-double-occupancy constraint for electrons. In terms of the on-site Hubbard U, the strengths of the exchange magnetic interactions are given by $J_a = (t_2^2 + t_{\text{so}}^2)/U$, $J_b = (t_2^2 - t_{\text{so}}^2)/U$, $J_1 = t_2^2/U$, $J^1_z = (t_1^2 - t_{\text{so}}^2)/U$, $J^2_z = (t_1^2 + t_{\text{so}}^2)/U$, and $J_2 = t_{\text{so}}^2/U$, with J_2 being the Dzyaloshinskii-Moriya (DM) interaction and the rest of the exchanges are the summation of the Heisenberg interaction and the spin dipole-dipole interaction.

From Eq. (8), it is clear that the DM interaction only appears along the z direction. Since the DM interaction tends to induce a magnetic spiral phase and the value of J^2_z is always larger than J^1_z, there should be competition between the spiral phase and the AFM/FM phase along the z direction. On the other hand, in the xy plane, the magnetic phase should be AFM or FM, since there are only Heisenberg interactions between nearest-neighbor sites. The value of J_a is always larger than J_b, therefore, FM holds the advantage in the xy plane.

To satisfy the no-double-occupancy constraint, Gutzwiller approximations are adopted by using the renormalized parameters [31]. In this approximation, the strength of the spin interaction remains the same as in the low-doping regime, and the operator $\tilde{C}_{i\sigma}$ is replaced by $C_{i\sigma}$. Therefore, the hopping Hamiltonian becomes

$$H'_t = \sum_{i\delta_z,\alpha} t'_1 C^{+}_{i,\alpha} C_{i+\delta_z\alpha} + \sum_{i\delta_x(y),\alpha} \alpha t'_2 C^{+}_{i,\alpha} C_{i+\delta_{x(y)}\alpha} - \frac{i}{2} t'_{\text{so}} \sum_{ij,\alpha\beta} \sigma C^{+}_{i,\alpha} C_{i\beta} + \text{H.c.}, \quad (9)$$

where $t'_1 = g_t t_1$, $t'_2 = g_t t_2$, and $t'_{\text{so}} = g_t t_{\text{so}}$ with $g_t = \frac{1-n}{1-2n_{i\uparrow}n_{i\downarrow}/n}$, n is the number of particles on site i (i.e., density of the particle number), and $n_{i\uparrow}$ and $n_{i\downarrow}$ are the numbers of particles for spin up and spin down electrons, respectively.

We shall compute the magnetic phase and electronic structures in a mean approximation with

$$S^{\alpha}_i S^{\beta}_j \approx S^{\alpha}_i \langle S^{\beta}_j \rangle + S^{\beta}_j \langle S^{\alpha}_i \rangle - \langle S^{\alpha}_i \rangle \langle S^{\beta}_j \rangle. \quad (10)$$

Here, the mean-field value of the magnetization on the i site, $\langle S_i \rangle$, is taken as a classical vector

$$\langle S_i \rangle = \mathbf{R} \cos(\mathbf{Q} \cdot r_i) + \mathbf{I} \sin(\mathbf{Q} \cdot r_i), \quad (11)$$

with $\mathbf{R} = (R^x, R^y, R^z)$ and $\mathbf{I} = (I^x, I^y, I^z)$ the mean-field parameters and $\mathbf{Q} = (Q_x, Q_y, Q_z)$ the magnetic wave vector. After performing the mean-field approximation and substituting Eq. (11) in the mean-field Hamiltonian, a discrete Fourier transformation

$$C_{k\sigma} = \frac{1}{\sqrt{N}} \sum_i \exp(i\mathbf{k} \cdot \mathbf{r}_i) \quad (12)$$

is performed, and the mean-field Hamiltonian becomes

$$H_{\text{MF}} = \sum_{\mathbf{k},\sigma} H'_t(\mathbf{k}) + H^{\text{MF}}_J. \quad (13)$$

Here, the hopping Hamiltonian is

$$\begin{aligned} H'_t(\mathbf{k}) = {} & [(t'_1 \cos k_z - \mu)\sigma_0 + t'_2(m + 2 - \cos k_x - \cos k_y)\sigma_z \\ & + t'_{\text{so}} \sin \mathbf{k} \cdot \boldsymbol{\sigma}]_{\sigma,\sigma'} C^{+}_{\mathbf{k}\sigma} C_{\mathbf{k}\sigma'} \\ & + \{[t'_1 \cos(k_z + Q_z) - \mu]\sigma_0 + t'_2[m + 2 \\ & - \cos(k_x + Q_x) - \cos(k_y + Q_y)]\sigma_z \\ & + t'_{\text{so}} \sin(\mathbf{k} + \mathbf{Q}) \cdot \boldsymbol{\sigma}\}_{\sigma,\sigma'} C^{+}_{\mathbf{k}+\mathbf{Q}\sigma} C_{\mathbf{k}+\mathbf{Q}\sigma'}, \end{aligned} \quad (14)$$

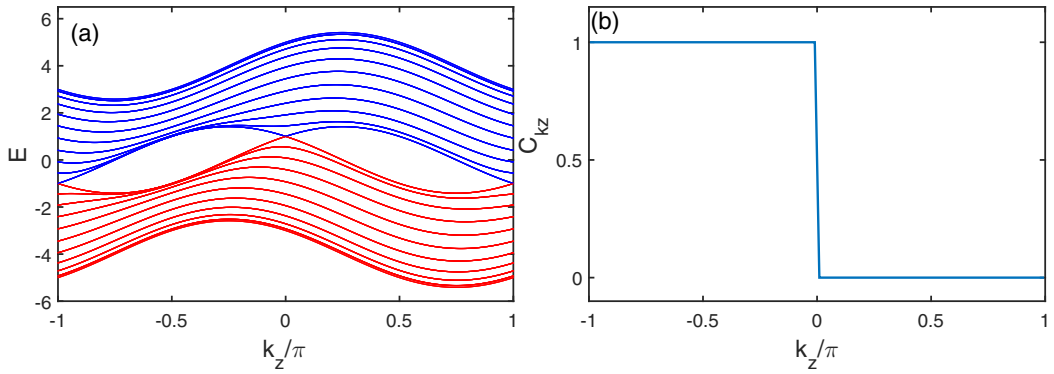

FIG. 1. (a) Band energies and (b) the Chern number C_{k_z} as a function of k_z with $U=0$, $m=0$, $t_1=1$, $t_2=1$, and $t_{\rm so}=1$, and $k_x=k_y$ in (a).

and the magnetic interaction is given by

$$H_J^{\rm MF} = \chi_1 C^+_{\mathbf{k}+\mathbf{Q}\uparrow} C_{\mathbf{k}\downarrow} + \chi_2 C^+_{\mathbf{k}+\mathbf{Q}\downarrow} C_{\mathbf{k}\uparrow} + \chi_3 (C^+_{\mathbf{k}+\mathbf{Q}\uparrow} C_{\mathbf{k}\uparrow} - C^+_{\mathbf{k}+\mathbf{Q}\downarrow} C_{\mathbf{k}\downarrow}) + \text{H.c.} + E^0_{\rm MF}, \quad (15)$$

where the parameters are

$$\chi_1 = \tfrac{1}{2}(A_1^+ \cos Q_x + A_2^+ \cos Q_y + A_3^- \cos Q_z + A_4^- \sin Q_z),$$
$$\chi_2 = \tfrac{1}{2}(A_1^- \cos Q_x + A_2^- \cos Q_y + A_3^+ \cos Q_z + A_4^+ \sin Q_z),$$
$$\chi_3 = \tfrac{1}{2}[A_5(\cos Q_x + \cos Q_y) + A_6 \cos Q_z], \quad (16)$$

with $A_1^\pm = \pm J_a(iR^y + I^y) - J_b(R^x - iI^x)$, $A_2^\pm = -J_a(R^x - iI^x) \pm J_b(iR^y + I^y)$, $A_3^\pm = J_z^1[(R^x - iI^x \pm (iR^y + I^y)]$, $A_4^\pm = J_2[\pm(R^x - iR^y) + (iI^x + I^y)]$, $A_5 = J_b(R^z - iI^z)$, and $A_6 = J_z^2(R^z - iI^z)$. The constant mean-field energy is

$$\begin{aligned} E^0_{\rm MF} = \tfrac{1}{2}[&(J_b \cos Q_x + J_a \cos Q_y)\Lambda_x \\ &+ (J_a \cos Q_x + J_b \cos Q_y)\Lambda_y \\ &- J_b(\cos Q_x + \cos Q_y)\Lambda_z] \\ &- \tfrac{1}{2}\left[J_z^1(\Lambda_x + \Lambda_y) + J_z^2 \Lambda_z\right] \cos Q_z \\ &- J_2(R^x I^y - R_y I^x) \sin Q_z, \end{aligned} \quad (17)$$

with $\Lambda_\alpha = (R^\alpha)^2 + (I^\alpha)^2$, $\alpha = x,y,z$.

The mean-field Hamiltonian can be generally expressed as

$$H_{\rm MF} = \sum_{\mathbf{k},\sigma} \psi^\dagger(\mathbf{k}) h_{\rm MF}(\mathbf{k}) \psi(\mathbf{k}), \quad (18)$$

with $h_{\rm MF}$ a 4×4 matrix and $\psi(\mathbf{k}) = (C_{\mathbf{k}\uparrow}, C_{\mathbf{k}\downarrow}, C_{\mathbf{k}+\mathbf{Q}\uparrow}, C_{\mathbf{k}+\mathbf{Q}\downarrow})^T$. From a given $h_{\rm MF}$, $\langle C^+_{\mathbf{k}\sigma} C_{\mathbf{k}\sigma'}\rangle$ and $\langle C^+_{\mathbf{k}+\mathbf{Q}\sigma} C_{\mathbf{k}\sigma'}\rangle$ are determined. The effective $\mathbf{R}$, $\mathbf{I}$, and $\mathbf{Q}$ are then self-consistent with the following self-consistent equations,

$$\frac{1}{N}\sum_{k\sigma} \langle C^+_{\mathbf{k}\sigma} C_{\mathbf{k}\sigma} + C^+_{\mathbf{k}+\mathbf{Q}\sigma} C_{\mathbf{k}+\mathbf{Q}\sigma}\rangle = n \quad (19)$$

and

$$R^\alpha = \text{Re}\left(\langle S^\alpha_Q\rangle\right), \quad I^\alpha = \text{Im}\left(\langle S^\alpha_Q\rangle\right), \quad (20)$$

where

$$\begin{aligned} S^x_Q &= \frac{1}{2}\sum_k (C^+_{\mathbf{k}\uparrow} C_{\mathbf{k}+\mathbf{Q}\downarrow} + C^+_{\mathbf{k}\downarrow} C_{\mathbf{k}+\mathbf{Q}\uparrow}), \\ S^y_Q &= \frac{1}{2i}\sum_k (C^+_{\mathbf{k}\uparrow} C_{\mathbf{k}+\mathbf{Q}\downarrow} - C^+_{\mathbf{k}\downarrow} C_{\mathbf{k}+\mathbf{Q}\uparrow}), \\ S^z_Q &= \frac{1}{2}\sum_k (C^+_{\mathbf{k}\uparrow} C_{\mathbf{k}+\mathbf{Q}\uparrow} - C^+_{\mathbf{k}\downarrow} C_{\mathbf{k}+\mathbf{Q}\downarrow}). \end{aligned} \quad (21)$$

Here, n is the density of the electron number. By minimizing the free energy, the optimal values of $\mathbf{R}$, $\mathbf{I}$, and $\mathbf{Q}$ are finally obtained.

III. MAGNETIC PHASE DIAGRAM AND TOPOLOGICAL ELECTRONIC STRUCTURES

In this section, we examine the magnetic phases that are allowed in the mean-field theory. For simplicity, we shall set $m=0$. For the case of $U=0$, two linear Weyl nodes are located at $\mathbf{k}=(0,0,0)$ and $\mathbf{k}=(0,0,\pi)$. The chirality of the Weyl node $\mathbf{k}=(0,0,0)$ is $+1$, since the effective Hamiltonian around which it can be written is $H = t_1 + t_{\rm so}\mathbf{k}\cdot\sigma$, while the chirality of $\mathbf{k}=(0,0,\pi)$ is -1. The band structure of $U=0$ and $m=0$ is shown in Fig. 1(a). It is clear that two Weyl points are separated in energy space due to the absence of inversion symmetry. If one fixes k_z, the Hamiltonian $H_{k_z}(k_x,k_y)$ can be viewed as a 2D system, which is gapped when $k_z \neq 0,\pi$. In this case, the Chern number C_{k_z} for a fixed k_z is well defined and can be computed as

$$C_{k_z} = \frac{1}{2\pi}\int_{\rm BZ} \Omega^{(n)}_{xy}(\mathbf{k}) dk_x dk_y, \quad (22)$$

where the Berry curvature is given by

$$\Omega^{(n)}_{xy}(\mathbf{k}) = -\text{Im}\left[\sum_{n'\neq n} \frac{\langle\psi_n(\mathbf{k})|\frac{\partial E_k}{\partial k_x}|\psi_{n'}(\mathbf{k})\rangle\langle\psi_{n'}(\mathbf{k})|\frac{\partial E_k}{\partial k_y}|\psi_n(\mathbf{k})\rangle}{[E_{n'}(\mathbf{k}) - E_n(\mathbf{k})]^2} - k_x \leftrightarrow k_y\right]. \quad (23)$$

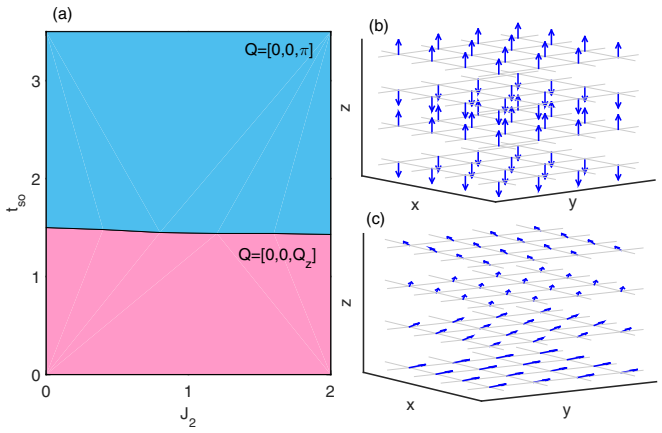

FIG. 2. (a) Magnetic phases of the Weyl semimetal in the strong correlation limit and the corresponding spin structures of (b) $Q = [0,0,\pi]$ (A-AFM phase)and (c) $Q = [0,0,Q_z]$ (SSDW phase) with $m = 0$ and $t_1 = t_2 = 1$. These magnetic phases are generic with the A-type AFM phase being expanded if the electron doping density increases.

Here, $E_n(\mathbf{k})$ and $\psi_n(\mathbf{k})$ are the nth eigenenergy and corresponding eigenstate for a given $\mathbf{k}$ in the Brillouin zone. Since the Weyl node is a magnetic monopole of the Berry curvature, the value of C_{k_z} jumps when one goes across Weyl nodes, and the Chern number of the Chern insulator equals the net monopole charge between the 2D system defining the trivial and Chern insulator. As shown in Fig. 1(b), $C_{k_z} = 0$ when $k_z \in (0,\pi)$, and $C_{k_z} = 1$ when $k_z \in (-\pi,0)$.

The magnetic phases in the strong correlation limit with $m = 0$ are shown in Fig. 2(a). We find that there are two distinct magnetic phases depending on the values of t_{so} and J_2 in the strong correlation limit. In the upper blue region, the magnetic wave vector Q is $[0,0,\pi]$. This is the A-AFM phase with the magnetic order between the nearest neighbors being FM in the xy plane and AFM between layers. In this phase, the spin orientation is along the $[0,0,1]$ direction, and the spin structure is shown in Fig. 2(b). Meanwhile, in the red region below, the magnetic wave vector Q is $[0,0,Q_z]$, with Q_z being a value that is incommensurate with the lattice and is along the $[0,0,1]$ direction. In this phase, spins are noncollinear and are in the SSDW phase, in which the spin orientation is in the xy plane and the direction of the spiral along the z axis is as shown in Fig. 2(c). The A-AFM and SSDW phases are two generic phases. When the electron doping density changes, both phases persist with one magnetic wave vector being fixed at $Q = [0,0,\pi]$ and the other one at $Q = [0,0,Q_z]$ with a slightly different Q_z. However, as the electron numbers increase, the A-AFM phase expands.

A. Topological electronic structures of the A-AFM phase

We now examine the band structure of the A-AFM phase. Since the spin orientation is always along the z direction in the A-AFM phase, the mean-field parameters in the x and y directions vanish, $R^x = I^x = R^y = I^y = 0$. In the basis of $\psi^\dagger = (C^\dagger_{\mathbf{k}\uparrow}, C^\dagger_{\mathbf{k}\downarrow}, C^\dagger_{\mathbf{k}+\mathbf{Q}\uparrow}, C^\dagger_{\mathbf{k}+\mathbf{Q}\downarrow})$, the magnetic interaction of

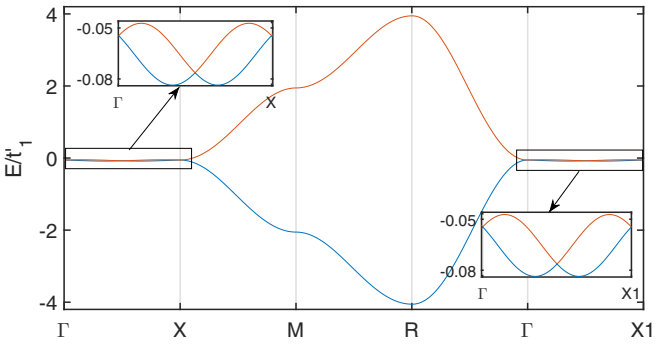

FIG. 3. Electronic structure of the A-AFM phase with $t_{so} = 2$ and $J_2 = 1$, displayed along the path: $\Gamma \to X$: $(0,0,\pi) \to M$: $(0,\pi,\pi) \to R$: $(\pi,\pi,\pi) \to \Gamma \to X1$: $(0,0,-\pi)$. The electronic structures around the four Weyl points $k = (0,0,0)$, $(0,0,\pi)$, and $(0,0,\pm\frac{1}{2}\pi)$ are shown in the insets.

the Hamiltonian Eq. (13) becomes

$$H_J^{\mathrm{MF}} = A(C^+_{\mathbf{k}\uparrow}C_{\mathbf{K}+\mathbf{Q}\uparrow} - C^+_{\mathbf{k}\downarrow}C_{\mathbf{K}+\mathbf{Q}\downarrow}) + \mathrm{H.c.} + E^0_{\mathrm{MF}}, \quad (24)$$

where $A = R^z(J_z^2 + 2J_b)/2$ is independent of $\mathbf{k}$. In this case, it is easy to see that two eigenvalues of the Hamiltonian matrix H_{MF} are around the value of $A + E^0_{\mathrm{MF}}$ and the other two are around the value of $-A + E^0_{\mathrm{MF}}$. Since A is much greater than t'_1, t'_2, and t'_{so} for the A-AFM phase, we find that the system is fully gapped with the lower two and upper two bands being separated by a gap of around $2A$.

In Fig. 3, we illustrate the structure of the lower two bands in the A-AFM phase with $t_{so} = 2$ and $J_2 = 1$. There are four touching points between the lower two bands, which are located at $\mathbf{k} = [0,0,0]$, $[0,0,\pi]$, and $[0,0,\pm\pi/2]$. These touching points are still the linear Weyl points with the monopole charge ± 1. To illustrate this, we plot the Chern number C_{k_z} in Fig. 4. It is seen that as k_z changes, whenever the energy bands touch, the corresponding Chern number also changes. Effectively, band inversion occurs as k_z changes. In the region $-\pi < k_z < -\pi/2$ and $0 < k_z < \pi/2$, the Hall conductance is quantized with $\sigma_{xy}(k_z) = e^2/\hbar C_{k_z}$. The changes in the Chern numbers crossing the Weyl points are always ± 1, which demonstrates that the monopole charges of Weyl nodes are ± 1.

In this phase, the magnetic ordering is similar to the proposed model of a magnetically doped multilayer

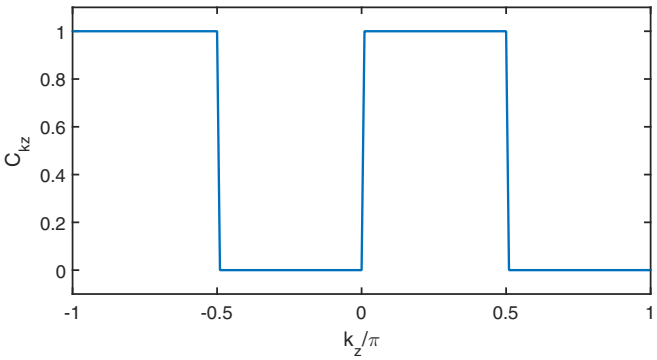

FIG. 4. Chern number C_{kz} of the A-AFM phase.

heterostructure composed of layers of normal and topological insulators [4]. However, different from the proposed model, the magnetic ordering between different layers is AFM for the A-AFM phase. Since the folding of the Brillouin zone occurs in the A-AFM phase, the interaction between the original Weyl nodes located at $k = (0,0,0)$ and $(0,0,\pi)$ can lead to new Weyl nodes.

B. Topological electronic structures of the $[0,0,Q_z]$ phase

In the SSDW phase, we have the mean-field parameters $R^z = I^z = 0$ and $R^x I^y + R^y I^x = 0$. As a result, the magnetic interaction of the mean-field Hamiltonian in the basis of $\Psi^\dagger = [C^\dagger_{\mathbf{k}\uparrow}, C^\dagger_{\mathbf{k}\downarrow}, C^\dagger_{\mathbf{k}+\mathbf{Q}\uparrow}, C^\dagger_{\mathbf{k}+\mathbf{Q}\downarrow}]$ becomes

$$H_J^{\mathrm{MF}} = B C^+_{\mathbf{k}\downarrow} C_{\mathbf{k}+\mathbf{Q}\uparrow} + \mathrm{H.c.} + E^0_{\mathrm{MF}}, \tag{25}$$

where $B = [J_z^1 \cos Q_z - J_2 \sin Q_z - (J_a + J_b)]R_x$ is independent of $\mathbf{k}$.

The eigenvalues of the Hamiltonian Eq. (25) can be approximately derived as

$$\begin{aligned}
E_k^1 &\approx t_1' \cos k_z + t_{\mathrm{so}}' \sin k_z + t_2'(2 - \cos k_x - \cos k_y) + E^0_{\mathrm{MF}},\\
E_k^2 &\approx t_1' \cos(k_z + Q_z) + t_{\mathrm{so}}' \sin(k_z + Q_z)\\
&\quad + t_2'(2 - \cos k_x - \cos k_y) + E^0_{\mathrm{MF}},\\
E_k^3 &\approx B + \tfrac{1}{2}[t_1' \cos k_z + t_1' \cos(k_z + Q_z)\\
&\quad - t_{\mathrm{so}}' \sin k_z + t_{\mathrm{so}}' \sin(k_z + Q_z)] + E^0_{\mathrm{MF}},\\
E_k^4 &\approx -B + \tfrac{1}{2}[t_1' \cos k_z + t_1' \cos(k_z + Q_z)\\
&\quad - t_{\mathrm{so}}' \sin k_z + t_{\mathrm{so}}' \sin(k_z + Q_z)] + E^0_{\mathrm{MF}}.
\end{aligned} \tag{26}$$

Therefore, in the SSDW phase, two electronic bands of the Weyl semimetal are around $\pm B$ and the middle two bands are around the chemical potential. Since B is much greater than t_1', t_2', and t_{so}' in the SSDW phase, the two energy bands around $\pm B + E^0_{\mathrm{MF}}$ are fully gapped, and the band touching points occur only between the two energy bands around the chemical potential. In Fig. 5, we show the electronic structures of the middle two bands near the chemical potential for $t_{\mathrm{so}} = 0.8$ and $J_2 = 1$. It is clear that two energy bands touch at two points along the z axis with $\mathbf{k} = [0,0,k_1]$ and $\mathbf{k} = [0,0,k_1 + \pi]$. Here, by using Eqs. (26), the nodal momentum k_1 is related to the magnetic wave vector as

$$k_1 = \tan^{-1} \frac{\cos Q_z - 1}{\sin Q_z}. \tag{27}$$

Around the band touching points, an effective 2×2 Hamiltonian can be found by taking only two bands near the Fermi energy. For this purpose, it is convenient to combine the magnetic mean-field Hamiltonian, Eq. (25), with the hopping Hamiltonian, Eq. (14). In the bias of $\Psi^+ = [C^+_{\mathbf{k}\uparrow}, C^+_{\mathbf{k}+\mathbf{Q}\downarrow}, C^+_{\mathbf{k}+\mathbf{Q}\uparrow}, C^+_{\mathbf{k}\downarrow}]$, around the Weyl node of $\mathbf{k} = (0,0,k_1)$, the Hamiltonian matrix h_{MF} can be written as

$$h_{\mathrm{MF}} = \begin{pmatrix} H_1 & V \\ V & H_2 \end{pmatrix}, \tag{28}$$

with

$$\begin{aligned}
H_1 &= [t_1'(\cos k_1 - q_z \sin k_1) + t_{\mathrm{so}}'(\sin k_1 + q_z \cos k_1)]\sigma_z^+\\
&\quad + [t_1'(\cos k_{Q1} - q_z \sin k_{Q1}) - t_{\mathrm{so}}'(\sin k_{Q1} + q_z \cos k_{Q1})]\sigma_z^-,\\
H_2 &= [t_1'(\cos k_{Q1} - q_z \sin k_{Q1}) + t_{\mathrm{so}}'(\sin k_{Q1} + q_z \cos k_{Q1})]\sigma_z^+\\
&\quad + [t_1'(\cos k_1 - q_z \sin k_1) - t_{\mathrm{so}}'(\sin k_1 + q_z \cos k_1)]\sigma_z^- + B\sigma_x,\\
V &= k_x \sigma_x + k_y \sigma_y.
\end{aligned} \tag{29}$$

Here, $\sigma_z^\pm = \frac{1}{2}(\sigma_0 \pm \sigma_z)$, $q_z = k_z - k_1$, and $k_{Q1} = k_1 + Q_z$. In Eq. (29), the dominant term is H_1. By treating V as the perturbation, in the second-order perturbation theory, the effective Hamiltonian around $\mathbf{k} = (0,0,k_1)$ is obtained as

$$\begin{aligned}
H_{\mathrm{eff}} &= H_1 - V H_2^{-1} V\\
&= -\frac{t_{\mathrm{so}}'^2}{B}(q_-^2 \sigma_+ + q_+^2 \sigma_-) + q_z(-t_1' \sin k_1 + t_{\mathrm{so}}' \cos k_1)\sigma_z\\
&\quad + (t_1' \cos k_1 + t_{\mathrm{so}}' \sin k_1)\sigma_0,
\end{aligned} \tag{30}$$

where $q_\pm = k_x \pm i k_y$ and $\sigma_\pm = \frac{1}{2}(\sigma_x \pm \sigma_y)$. Similarly, following the same procedure, the effective Hamiltonian around the other Weyl node $\mathbf{k} = (0,0,k_1 + \pi)$ can be also obtained in the same way.

As pointed in Ref. [16], the effective Hamiltonian, Eq. (30), describes a Weyl node carrying a monopole charge of -2, which is protected by C_6 symmetry. Indeed, as shown in Fig. 6, we plot the Chern number C_{k_z}. It is seen that as k_z changes, whenever the energy bands touch, the corresponding Chern number also changes. Effectively, band inversion occurs as

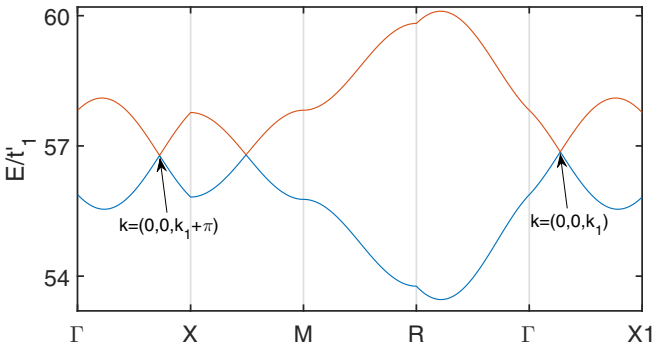

FIG. 5. Electronic structure of the SSDW phase, displayed along the path: $\Gamma \to X$: $(0,0,\pi) \to M$: $(0,\pi,\pi) \to R$: $(\pi,\pi,\pi) \to \Gamma \to X1$: $(0,0,-\pi)$. Here, the optimal Q is $[0,0,0.55\pi]$, and $k_1 = -0.275\pi$.

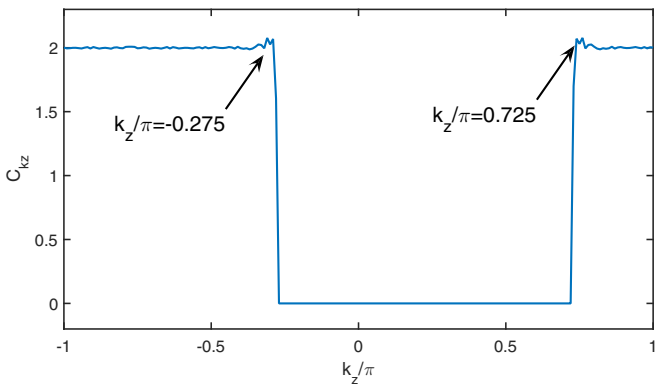

FIG. 6. Chern number C_{k_z} as a function of k_z for the SSDW phase.

k_z changes. In the region $-\pi < k_z < -k_1$ and $k_1 < k_z < \pi$, the Hall conductance is quantized with $\sigma_{xy}(k_z) = 2e^2/h$. The changes in the Chern numbers crossing the Weyl points are always ± 2, which demonstrates that monopole charges of the Weyl nodes are ± 2. Hence the pair of Weyl nodes are double-split Weyl nodes. In this SSDW phase, the spin ordering cannot break the C_4 rotation symmetry, which means such double-Weyl nodes are not protected by rotation symmetry. Therefore, as the spin-orbit interaction increases, a magnetic transition occurs with the magnetic order being turned into the A-AFM order, which breaks the rotational symmetry of the SSDW phase. As a result, the double-Weyl nodes at $(0,0,\pm k_1)$ are no longer stable [16] and are split into four single-Weyl nodes, located at (0,0,0), $(0,0,\pm\pi/2)$, and $(0,0,\pi)$.

IV. DISCUSSION AND CONCLUSION

In conclusion, we have explored the magnetic phase and the corresponding topological electric structures of the Weyl semimetal in the strong on-site Hubbard U limit. For the minimum model of a Weyl semimetal that possesses two linear Weyl nodes, the magnetic phases in the small-U regime can be also analyzed in the mean-field approximation. In this case, the order parameters at site i are defined as $\langle S_i^+\rangle = \langle C_{i\uparrow}^\dagger C_{i\downarrow}\rangle$, $\langle S_i^-\rangle = \langle C_{i\downarrow}^\dagger C_{i\uparrow}\rangle$, and $\langle S_i^z\rangle = \langle (n_{i\uparrow} - n_{i\downarrow})/2\rangle$. The mean-field Hamiltonian is given by

$$\begin{aligned} H_M = {} & E_{\rm HF}^0 + \sum_{\mathbf{k},\alpha,\beta} C_\alpha^\dagger(\mathbf{k}) H_{0,\alpha\beta}(\mathbf{k}) C_\beta(\mathbf{k}) \\ & - \frac{1}{3}U \sum_{\mathbf{k}} [\gamma_1 C_{\mathbf{k}+\mathbf{Q}\downarrow}^+ C_{\mathbf{k}\uparrow} + \gamma_2 C_{\mathbf{k}\downarrow}^+ C_{\mathbf{K}+\mathbf{Q}\uparrow} \\ & + \gamma_3 C_{\mathbf{k}+\mathbf{Q}\uparrow}^+ C_{\mathbf{k}\uparrow} - \gamma_3 C_{\mathbf{k}+\mathbf{Q}\downarrow}^+ C_{\mathbf{K}\downarrow} + \text{H.c.}]. \end{aligned} \quad (31)$$

Here, $E_{\rm MF}^0 = nU/2 + (\Lambda_x^2 + \Lambda_y^2 + 2\Lambda_z^2)/6$, $\gamma_1 = R_x + I_y + iR_y - iI_x$, $\gamma_2 = R_x - I_y + iR_y + iI_x$, $\gamma_3 = R_z - iI_z$, and H_0 is given by Eq. (2) with R_α and I_α as in Eq. (11) and $\Lambda_\alpha = (R_\alpha)^2 + (I_\alpha)^2$. Figure 7 illustrates a possible phase in the weak on-site interaction regime. It is seen that when U/t_1 is smaller than 3.5, the Weyl semimetal is in the paramagnetic (PM) phase. In the PM phase, the topological properties of the band structure are unchanged. When U/t_1 is larger than 3.5 and $t_{\rm so}$ is small, the A-AFM phase emerges. However, the A-AFM phase is different from the A-AFM phase in the strong correlation limit. The staggered magnetization lies in the xy plane for the A-AFM phase in the weak interacting regime and is denoted as the A-AFM xy phase. Hence it is clear that when the on-site U is turned on, the Weyl semimetal is paramagnetic without magnetic orders. The electronic structure is similar to that of the noninteracting Weyl fermions with the parameters being just renormalized. As U increases and is strong enough, the Weyl semimetal starts to become magnetic. The increase of U tends to first stabilize the A-AFM xy phase due to its commensurate nature. As U becomes large, the Dzyaloshinskii-Moriya interaction is induced so that the spiral spin density wave (SSDW) state starts to emerge. Only in the strong on-site U limit are both the SSDW state and A-AFM phases stabilized.

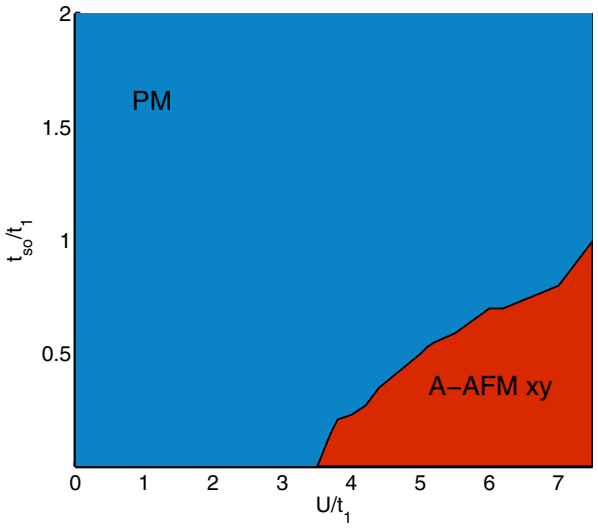

FIG. 7. Magnetic phases of the Weyl semimetal at half filling ($n = 1$) in the weak on-site interaction regime. Here, the blue region is the paramagnetic phase. The red region is the A-AFM phase with staggered magnetization in the xy plane.

In the strong-U limit, we have derived an extended t-J model. The mean-field phase diagram in the large-U limit of the Hubbard model is established. We show that due to the Dzyaloshinskii-Moriya interaction induced by the spin-orbit interaction, the A-AFM phase and the SSDW phase are two generic magnetic phases. As the spin-orbit coupling increases, a quantum phase transition occurs with the SSDW phase turning into an A-AFM phase. In addition, it is shown that the topology of the electronic structure also undergoes changes as the magnetic phase changes. In the A-AFM phase, the number of linear Weyl nodes increases due to the folding of the Brillouin zone, while for the SSDW phase, linear Weyl nodes combine and are turned into double-Weyl nodes carrying a monopole charge of ± 2. It should be noted that, while in the small-U regime, the Weyl semimetal can be either in the paramagnetic (PM) phase or in the A-AFM phase with spin in the xy plane. However, these phases cannot lead to a significant change in the topological properties of the Weyl semimetal. The increase of U tends to stabilize the spiral spin density wave (SSDW) state and A-AFM phase and increases the magnetic energy gain. Strong magnetization can lead to a significant change in the topological properties of the Weyl semimetal. Our findings thus pave a way to build a double-Weyl semimetal from a Weyl semimetal.

While so far in this work we only considered Weyl semimetals with two linear Weyl nodes located along the z axis, due to the rotational invariance of the Hubbard interaction, we expect that the results may be applicable to pairs of Weyl nodes located along other axes. In general, the number of linear Weyl nodes may exceed two. Our results are applicable to any pair of linear Weyl nodes located along some axis passing through the Γ point. Thus, we expect our findings of the unusual interplay between the topology of electronic structures and magnetism may be applicable to Weyl semimetals with more than two Weyl nodes.

Even though our results are based on the mean-field theory, the Weyl points in the electronic structures have a topological origin, which is reflected in their origin from the band inversion along the z axis. Hence it is expected that the topological electronic structures of the nodes are robust even if magnetic fluctuations are included. In real materials, the exact electronic structure depends on detailed crystal symmetries and may show different detailed structures. Nonetheless, our results offer an important direction to look for in the interplay between magnetic phases and electronic structures and are left for future experimental confirmations.

ACKNOWLEDGMENTS

This work was supported by the Ministry of Science and Technology (MoST), Taiwan. We also acknowledge support from TCECM and Academia Sinica Research Program on Nanoscience and Nanotechnology, Taiwan.

[1] M. Z. Hasan and C. L. Kane, Rev. Mod. Phys. **82**, 3045 (2010).
[2] M. Z. Hasan and J. E. Moore, Annu. Rev. Condens. Matter Phys. **2**, 55 (2011).
[3] S. Murakami, New J. Phys. **9**, 356 (2007); L. Balents, Physics **4**, 36 (2011).
[4] A. A. Burkov and L. Balents, Phys. Rev. Lett. **107**, 127205 (2011).
[5] X. Wan, A. M. Turner, A. Vishwanath, and S. Y. Savrasov, Phys. Rev. B **83**, 205101 (2011).
[6] P. Hosur and X. Qi, C. R. Phys. **14**, 857 (2013).
[7] Z. Wang, Y. Sun, X.-Q. Chen, C. Franchini, G. Xu, H. Weng, X. Dai, and Z. Fang, Phys. Rev. B **85**, 195320 (2012).
[8] A. H. Castro Neto, F. Guinea, N. M. R. Peres, K. S. Novoselov, and A. K. Geim, Rev. Mod. Phys. **81**, 109 (2009).
[9] P.-H. Chou, L.-J. Zhai, C.-H. Chung, C.-Y. Mou, and T.-K. Lee, Phys. Rev. Lett. **116**, 177002 (2016).
[10] Z. K. Liu, B. Zhou, Y. Zhang, Z. J. Wang, H. M. Weng, D. Prabhakaran, S.-K. Mo, Z. X. Shen, Z. Fang, X. Dai, Z. Hussain, and Y. L. Chen, Science **343**, 864 (2014).
[11] D. Xiao, M.-C. Chang, and Q. Niu, Rev. Mod. Phys. **82**, 1959 (2010).
[12] K. Kobayashi, T. Ohtsuki, K.-I. Imura, and I. F. Herbut, Phys. Rev. Lett. **112**, 016402 (2014).
[13] P. Goswami and S. Chakravarty, Phys. Rev. Lett. **107**, 196803 (2011).
[14] B.-L. Huang and C.-Y. Mou, Europhys. Lett. **88**, 68005 (2009); B.-L. Huang, M.-C. Chang, and C.-Y. Mou, Phys. Rev. B **82**, 155462 (2010); S.-T. Lee, S.-M. Huang, and C.-Y. Mou, J. Phys.: Condens. Matter **26**, 255502 (2014).
[15] L. X. Yang *et al.*, Nat. Phys. **11**, 728 (2015).
[16] C. Fang, M. J. Gilbert, X. Dai, and B. A. Bernevig, Phys. Rev. Lett. **108**, 266802 (2012).
[17] G. Xu, H. Weng, Z. Wang, X. Dai, and Z. Fang, Phys. Rev. Lett. **107**, 186806 (2011).
[18] S.-K. Jian and H. Yao, Phys. Rev. B **92**, 045121 (2015).
[19] M.-C. Chang and M.-F. Yang, Phys. Rev. B **92**, 205201 (2015).
[20] H.-H. Lai, Phys. Rev. B **91**, 235131 (2015); S. M. Huang, S.-Y. Xu, I. Belopolski, C.-C. Lee, G. Chang, T.-R. Chang, B. K. Wang, N. Alidoust, G. Bian, M. Neupane, D. Sanchez, H. Zheng, H.-T. Jeng, A. Bansil, T. Neupert, H. Lin, and M. Zahid Hasan, Proc. Natl. Acad. Sci. USA **113**, 1180 (2016).
[21] S.-L. Yu, X. C. Xie, and J.-X. Li, Phys. Rev. Lett. **107**, 010401 (2011).
[22] Y. Yamaji and M. Imada, Phys. Rev. B **83**, 205122 (2011).
[23] T. Yoshida, S. Fujimoto, and N. Kawakami, Phys. Rev. B **85**, 125113 (2012).
[24] S.-M. Huang, S.-T. Lee, and C.-Y. Mou, Phys. Rev. B **89**, 195444 (2014).
[25] D. E. Sheehy and J. Schmalian, Phys. Rev. Lett. **99**, 226803 (2007).
[26] A. Sekine and K. Nomura, Phys. Rev. B **90**, 075137 (2014).
[27] H. Wei, S.-P. Chao, and V. Aji, Phys. Rev. B **89**, 235109 (2014).
[28] M.-C. Chang and M.-F. Yang, Phys. Rev. B **91**, 115203 (2015).
[29] X.-L. Qi, Y.-S. Wu, and S.-C. Zhang, Phys. Rev. B **74**, 085308 (2006).
[30] J.-T. Kao, S.-M. Huang, C.-Y. Mou, and C. C. Tsuei, Phys. Rev. B **91**, 134501 (2015).
[31] B. Edegger, V. N. Muthukumar, and C. Gros, Adv. Phys. **56**, 927 (2007).